

Effects of beam spinning on the fourth-order particle resonance of 3D bunched beams in high-intensity linear accelerators

Yoo-Lim Cheon[✉], Seok-Ho Moon, and Moses Chung^{✉*}

*Intense Beam and Accelerator Laboratory, Department of Physics,
Ulsan National Institute of Science and Technology, Ulsan 44919, Republic of Korea*

Dong-O Jeon^{✉†}

Rare Isotope Science Project, Institute for Basic Science, Daejeon 34047, Republic of Korea

 (Received 23 February 2022; accepted 31 May 2022; published 10 June 2022)

The aim of this study is to make the parameter space of zero-current phase advance greater than 90° available to the high-intensity linear accelerator (linac) design and operation, which has been excluded to avoid the envelope instabilities and particle resonances. The earlier study of Cheon *et al.* [*Nucl. Instrum. Methods Phys. Res., Sect. A* **1013**, 165647 (2021)] reported that the spinning of ion beams can mitigate the fourth-order particle resonance and the associated envelope instability in high-intensity linacs. In the present work, we further investigate the effects of beam spinning on the fourth-order particle resonance in the case of 3D bunched beams with fast acceleration. We also explore the space-charge-driven resonance in the longitudinal plane and confirm that the fourth-order particle resonance can be manifested when the longitudinal zero-current phase advance σ_{z0} is larger than 90° and the depressed phase advance σ_z is less than 90° , similar to the transverse case. The beam spinning effects are examined in both transverse and longitudinal planes during beam acceleration through periodic solenoid and quadrupole-doublet focusing channels.

DOI: [10.1103/PhysRevAccelBeams.25.064002](https://doi.org/10.1103/PhysRevAccelBeams.25.064002)

I. INTRODUCTION

Charged particle beam physics to understand beam instabilities and halo formation mechanisms in high-intensity linear accelerators (linacs) has been actively studied over the past 50 years. In early days, only parametric instabilities of space charge were known to the community, and the first experimental hints for emittance growth due to zero-current phase advance (σ_0) above 90° were published in 1985 [1]. In 2009, the fourth-order particle resonance in the linac was discovered [2], which was experimentally verified in the GSI Universal Linear Accelerator [3] and later in the Spallation Neutron Source (SNS) linac [4]. Since then, it has been considered that, in linacs, the space-charge-driven $4\sigma = 360^\circ$ (or 4:1) fourth-order particle resonance [2–8] together with the well-known envelope instability [9–13] sets the main operational limits and that the zero-current phase advance σ_0 should be less than 90° . Therefore,

studies on how to overcome this operational limit are essential for expanding the range of choices for focusing parameters and beam currents in accelerator design.

In our previous study [14], we proposed the novel approach of using spinning ion beams to mitigate the space-charge-driven $4\sigma = 360^\circ$ fourth-order particle resonance in high-intensity linacs. Here, σ is the depressed phase advance per lattice period. It has been found that spinning beams have an intrinsic characteristic that can mitigate fourth-order resonance and subsequent envelope instability, which indeed reduces emittance growth and the evolution of halo particles. We investigated the spinning effects using both analytical and multiparticle simulation studies for 2D coasting beams in a solenoid focusing channel.

The spinning ion beam concept appears to be similar to the magnetized electron beam (or angular-momentum-dominated electron beam), which has been applied in enhancing the efficiency of electron cooling or in generating flat beams for certain applications [15–18]. However, we emphasize that the main purpose of beam spinning in our previous study was to mitigate space charge effects in the ion beam itself; thus, the scope of beam physics therein is different from the electron beam case.

Recently, Qiang reported [19] that envelope instability for $\sigma_0 > 90^\circ$ can be mitigated in high-intensity linacs by passing through the envelope instability stop band quickly using a fast acceleration scheme. Nevertheless, even with

*Corresponding author.
mchung@unist.ac.kr

†Corresponding author.
jeond@ibs.re.kr

Published by the American Physical Society under the terms of the Creative Commons Attribution 4.0 International license. Further distribution of this work must maintain attribution to the author(s) and the published article's title, journal citation, and DOI.

fast acceleration, the fourth-order particle resonance would inevitably manifest over short periods and still remain an important source for inducing emittance growth and halo formations. We note that the fourth-order resonance stop band is wider than the envelope instability stop band [20].

Hence, in this paper, we investigate the beam spinning effects on the $4\sigma = 360^\circ$ fourth-order particle resonance in the presence of fast acceleration using more realistic 3D bunched beams. In this study, we envision that envelope instability is handled mainly by fast acceleration, whereas the fourth-order particle resonance is mitigated by beam spinning. As longitudinal dynamics is involved in this study, we also explore the possibility of a space-charge-driven fourth-order resonance in the longitudinal plane. In addition to the solenoid focusing lattice, we also consider the quadrupole-doublet focusing lattice in multiparticle simulations.

First, we briefly summarize the basic concepts and physical models in Sec. II. In Secs. III A and III B, the spinning effect on the fourth-order resonance in the transverse plane is covered for cases with and without acceleration. For spinning beams, coupling between transverse degrees of freedom reduces the resonance driving effect [14] and weakens the fourth-order resonant structure, resulting in the suppression of emittance growth and halo evolution. In Sec. IV, the spinning effects on the fourth-order resonance in the longitudinal plane are discussed. We found that fourth-order particle resonance is also observed in the longitudinal phase space, in which it is generated mainly from the longitudinal nonlinear space charge field. Although the beam spinning effect is considerable in the transverse plane, it does not evidently affect the longitudinal dynamics. Summary and discussions are given in Sec. V.

II. BACKGROUND

A spinning beam has a nonzero average canonical angular momentum in the transverse plane, $\langle P_\theta \rangle = \langle \beta\gamma mc \rangle \langle xy' - yx' \rangle$ (for the drift space where vector potential vanishes), and exhibits rigid rotor rotation around the beam propagation axis [14,21]. Here, $\gamma = (1 - \beta^2)^{-1/2}$ is the relativistic mass factor with $\beta = v/c$, where v is the beam velocity and c is the speed of light in vacuum. Brackets $\langle \dots \rangle$ denote the statistical average over the beam distribution; x and y are the transverse degrees of freedom of a single particle; and $\{ \}' \equiv \frac{d}{ds}$ is a derivative with respect to the axial coordinate s . For a nonspinning beam, the transverse rms emittance is equal to the thermal emittance $\epsilon_{\text{rms},\perp} = \epsilon_{\text{th},\perp} = \sqrt{\det(\Sigma)}$, which is related to the determinant of the 4×4 beam matrix $\Sigma = \langle zz^T \rangle$, where $z = (x, y, x', y')^T$ with $(\dots)^T$ being the transpose operation. For a spinning beam with axisymmetry, the transverse rms emittance $\epsilon_{\text{rms},\perp} = \sqrt{\epsilon_{\text{th},\perp}^2 + \langle \hat{P}_\theta \rangle^2 / 4}$ is composed of the

transverse thermal emittance $\epsilon_{\text{th},\perp}$, and the normalized average canonical angular momentum $\langle \hat{P}_\theta \rangle = \langle \frac{P_\theta}{\beta\gamma mc} \rangle$ [14].

To generate spinning beams in multiparticle simulations, we launch initial beam particles around the center of a solenoid under the magnetic field B_z without any average rotation. Then, the initial canonical angular momentum is given by the function of the radial coordinate r as $P_\theta = qB_z(s=0)r^2/2$. When the beam passes out of the solenoid, where $B_z = 0$, the canonical angular momentum becomes $P_\theta = \beta\gamma mc(xy' - yx') = \beta\gamma mc r^2 \theta'$, and the beam has azimuthal rotation in θ [17,22]. We propagate this spinning beam through a periodic focusing channel with initially well-matched conditions. In the actual experimental setting, a rotating ion beam was generated by stripping an ion beam inside a solenoid for the emittance transfer experiment at GSI [23].

In this study, we are dealing with a 3D bunched beam of spheroidal Gaussian density distribution, which is the main cause of the fourth-order particle resonance in both transverse and longitudinal planes. For reference purposes, we write the equations of motion for a single particle of a 3D axisymmetrical bunched beam under solenoid focusing with the canonical angular momentum in the laboratory frame, which are given by [14,24,25]

$$r''(s) + \kappa_\perp(s)r(s) - \frac{\hat{P}_\theta^2}{r^3(s)} - \frac{q^2 N}{2\pi\epsilon_0\beta^2\gamma^3 mc^2} r(s) A_\perp(s) = 0 \quad (1)$$

and

$$\zeta''(s) + \kappa_\parallel(s)\zeta(s) - \frac{q^2 N}{2\pi\epsilon_0\beta^2\gamma^3 mc^2} \zeta(s) A_z(s) = 0, \quad (2)$$

where r is the radial coordinate and $\zeta = z - z_s$ is the longitudinal coordinate that denotes the deviation away from a synchronous particle at z_s . Here, N is the number of beam particles in a bunch, ϵ_0 is the vacuum permittivity, $\kappa_\perp(s)$ is the transverse focusing coefficient as a function of the axial coordinate s , and $\kappa_\parallel(s) = \frac{2\pi q E_0 T (-\sin\phi_s)}{\lambda_{\text{rf}} \beta^3 \gamma^3 mc^2}$ is the longitudinal rf focusing coefficient, where λ_{rf} is the radio-frequency (rf) wavelength, $E_0 T$ is the effective accelerating field, and ϕ_s is the synchronous phase. The average (macropulse) beam current is calculated by $I = qNc/\lambda_{\text{rf}}$. For our multiparticle simulations, we use 175 MHz of rf frequency and $\lambda_{\text{rf}} = 1.713$ m. The total number of particles in a bunch scales is $N = 3.566 \times 10^7$ for $I = 1$ mA of beam current.

Also,

$$A_\perp(s) = \int_0^\infty \frac{d\chi}{\{R^2(s) + \chi\}^2 \{2\gamma^2 Z^2(s) + \chi\}^{1/2}} \times \frac{\gamma}{\sqrt{\pi}} e^{-r^2(s)/\{R^2(s) + \chi\} - \gamma^2 \zeta^2(s)/\{2\gamma^2 Z^2(s) + \chi\}} \quad (3)$$

and

$$A_z(s) = \int_0^\infty \frac{d\chi}{\{R^2(s) + \chi\}\{2\gamma^2 Z^2(s) + \chi\}^{3/2}} \times \frac{\gamma}{\sqrt{\pi}} e^{-r^2(s)/\{R^2(s)+\chi\} - \gamma^2 \zeta^2(s)/\{2\gamma^2 Z^2(s)+\chi\}} \quad (4)$$

represent the space charge fields of a 3D bunched spheroidal Gaussian density beam in the laboratory frame as functions of the rms radial beam size $R(s)$ and the rms longitudinal beam size $Z(s)$, respectively [25,26]. The phase advances of an entire beam distribution are defined by $\sigma_\perp = \int_0^S \epsilon_{\text{rms},\perp} \frac{ds}{R^2(s)/2}$ and $\sigma_z = \int_0^S \epsilon_{\text{rms},z} \frac{ds}{Z^2(s)}$, where S is the length of lattice period and $\epsilon_{\text{rms},z}$ is the longitudinal rms emittance.

Note that, in Eq. (2), we neglect the nonlinear term associated with the rf fields, which could be significant for large amplitude longitudinal motions [27]. In Sec. IV, nevertheless, we found that nonlinear effects in the longitudinal plane are dominated by the space charge field A_z for high-intensity beams.

For an infinitely long Gaussian beam with $Z(s) \rightarrow \infty$, Eq. (1) becomes

$$r''(s) + \kappa_\perp(s)r(s) - \frac{\hat{P}_\theta^2}{r^3(s)} - K \frac{1 - e^{-[r^2(s)/R^2(s)]}}{r(s)} = 0, \quad (5)$$

which is Eq. (2) in Ref. [14]. Here, $K = \frac{q\lambda}{2\pi\epsilon_0\beta^2\gamma^3 mc^2}$ [in meter-kilogram-second system (MKS) of units] is the space charge perveance, and $\lambda = \frac{q}{\sqrt{2\pi}} \frac{N}{Z}$ is the line charge density [28].

When $\hat{P}_\theta = 0$, the nonlinear space charge term produces an octupole that drives the 4:1 resonance [2,29,30]. When $\hat{P}_\theta \neq 0$, the third term in Eq. (5) prevents the radial coordinate of each particle from surpassing $r = 0$ [24]; furthermore, it introduces a coupling between the transverse degrees of freedom and reduces the fourth-order resonance driving effect, making the space-charge-driven resonance structures blurred (see the appendix in Ref. [14] for the detailed analytic interpretation).

Solenoids and quadrupole doublets are considered for transverse focusing, and rf cavities are used for longitudinal focusing and acceleration. The periodic lattices used for the 3D bunched beam simulations are shown in Figs. 1 and 2. The length of the lattice period is $S = 661$ mm for a channel with a solenoid and rf cavity and $S = 500$ mm for a channel with a quadrupole doublet and rf cavity. Under solenoid focusing, axisymmetric beam propagation is possible along the linac. For the quadrupole doublet, the focusing (F) and defocusing (D) quadrupoles have the same magnitude in terms of focusing strength.

Figure 3 shows the variations of $\langle \hat{P}_\theta \rangle$ without acceleration (upper plots) and $\beta\gamma\langle \hat{P}_\theta \rangle$ as the beam is accelerated from $\beta = 0.1028$ to $\beta = 0.17$ (lower plots), along the

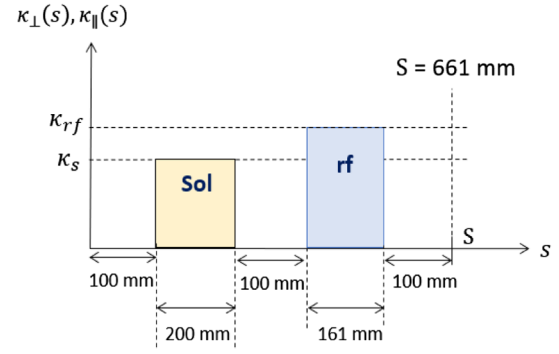


FIG. 1. Periodic focusing lattice composed of a solenoid and an rf cavity. The length of the lattice period is $S = 661$ mm. Under solenoid focusing, axisymmetric beam propagation is possible along the linac.

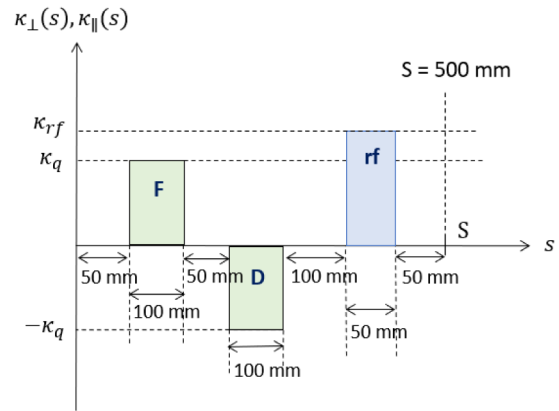


FIG. 2. Periodic focusing lattice composed of a quadrupole doublet and an rf cavity. The length of the lattice period is $S = 500$ mm. The focusing (F) and defocusing (D) quadrupoles have the same magnitude of focusing strength.

solenoid and quadrupole-doublet focusing channels. Here, we multiply $\beta\gamma$ for cases with acceleration to consider that the beam divergences x' and y' are reduced during acceleration. The average canonical angular momentum is calculated over 100 000 macroparticles. The initial transverse tune depression is $\sigma_\perp/\sigma_{\perp 0} = 0.78$ with $\sigma_{\perp 0} = 100^\circ$ and $\sigma_\perp = 78^\circ$ for the beams without acceleration and $\sigma_\perp/\sigma_{\perp 0} = 0.7$ with $\sigma_{\perp 0} = 110^\circ$ and $\sigma_\perp = 76^\circ$ for the beams with acceleration.

In Fig. 3(a), which shows the case with solenoid focusing, both $\langle \hat{P}_\theta \rangle$ and $\beta\gamma\langle \hat{P}_\theta \rangle$ are conserved, because the beam is axisymmetric. However, as illustrated in Fig. 3(b), which shows the case with quadrupole focusing, both $\langle \hat{P}_\theta \rangle$ and $\beta\gamma\langle \hat{P}_\theta \rangle$ are not conserved. Although the canonical angular momentum is not conserved with quadrupoles, beam spinning effects are still observable to some degree in the fourth-order particle resonance in the transverse phase space (see Secs. III A and III B for detailed discussions).

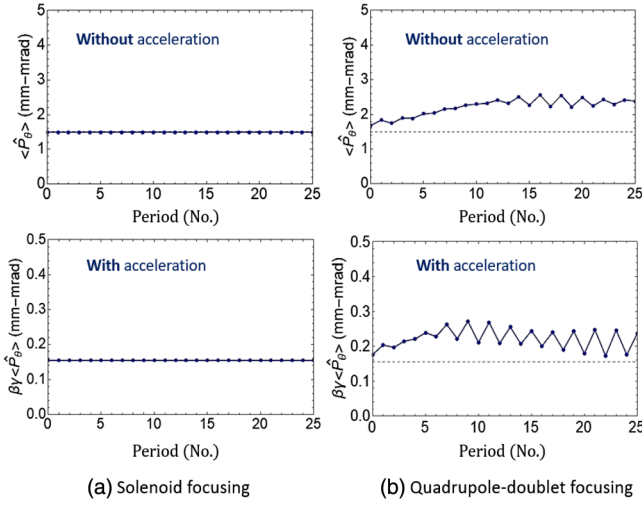


FIG. 3. The plots of $\langle \hat{P}_\theta \rangle$ change without acceleration (upper plots) and $\beta\gamma\langle \hat{P}_\theta \rangle$ change as the beam is accelerated from $\beta = 0.1028$ to $\beta = 0.17$ (lower plots) along (a) the solenoid focusing channel and (b) the quadrupole-doublet focusing channel. Whereas $\langle \hat{P}_\theta \rangle$ and $\beta\gamma\langle \hat{P}_\theta \rangle$ are conserved in solenoid lattices, they are not conserved in quadrupole lattices. The initial transverse tune depression is $\sigma_\perp/\sigma_{\perp 0} = 0.78$ and 0.7 for the beams without and with acceleration, respectively.

III. FOURTH-ORDER PARTICLE RESONANCE IN TRANSVERSE SPACE

The $\sigma_{\perp 0} = 90^\circ$ has been the limit in high-intensity linac design and operation. Efforts to surpass this operational limit have been in progress to achieve a much higher beam current for future applications such as intensity-frontier particle and nuclear physics experiments, fusion material irradiation tests, nuclear waste transmutation, and accelerator-driven subcritical reactors.

When $\sigma_{\perp 0} > 90^\circ$, the well-known envelope instabilities are triggered by perturbed oscillations of envelope modes [i.e., breathing (B) and quadrupole (Q) modes] [11], and the corresponding emittance growth is observed over long lattice periods. On the other hand, as discussed in Ref. [20], the fourth-order particle resonance is manifested over short periods even for the initially well-matched Gaussian beams before the envelope instability is generated. Also, the stop band of the fourth-order resonance is $\sigma_{\perp 0} > 90^\circ$ and $\sigma_\perp < 90^\circ$, which is wider than the envelope instability stop band.

Focusing on this point, here we investigate the novel approach to mitigate the fourth-order particle resonance by applying the spinning for more realistic 3D bunched beams in linacs. The spinning beams have an intrinsic characteristic of mitigating the fourth-order resonance, resulting in the suppression of emittance growths and halo formations. Note that what we present in our simulation studies are the projected rms emittances in laboratory planes, not the eigenemittances.

A. Spinning effects without acceleration

First, in this section, we describe multiparticle simulation results for investigating the effects of spinning on the fourth-order particle resonance in the transverse plane without acceleration. Throughout this study, we use the TraceWin code [31]. Fourth-order particle resonance occurs in the transverse space under the conditions of $\sigma_{\perp 0} > 90^\circ$ and $\sigma_\perp < 90^\circ$. Here, $\sigma_{\perp 0}$ (σ_\perp) denotes the transverse zero-current (depressed) phase advance per lattice period.

Figure 4 shows the relative emittance growth over 20 periods in the transverse tune depression space ($\sigma_\perp/\sigma_{\perp 0}$) and the phase-space plots under the solenoid focusing lattice without acceleration. The relative emittance growth is defined as the ratio of the final projected rms emittance ($\epsilon_{\text{rms},f}$) to the initial projected rms emittance ($\epsilon_{\text{rms},i}$), that is, $\epsilon_{\text{rms},f}/\epsilon_{\text{rms},i}$. During 20 periods, fourth-order particle resonance predominantly occurs, and the emittance growth is mainly affected by the fourth-order resonance under well-matched conditions.

Here, the zero-current phase advances are $\sigma_{\perp 0} = 100^\circ$ in the transverse space and $\sigma_{z0} = 30^\circ$ in the longitudinal space, whereby there is no emittance exchange between

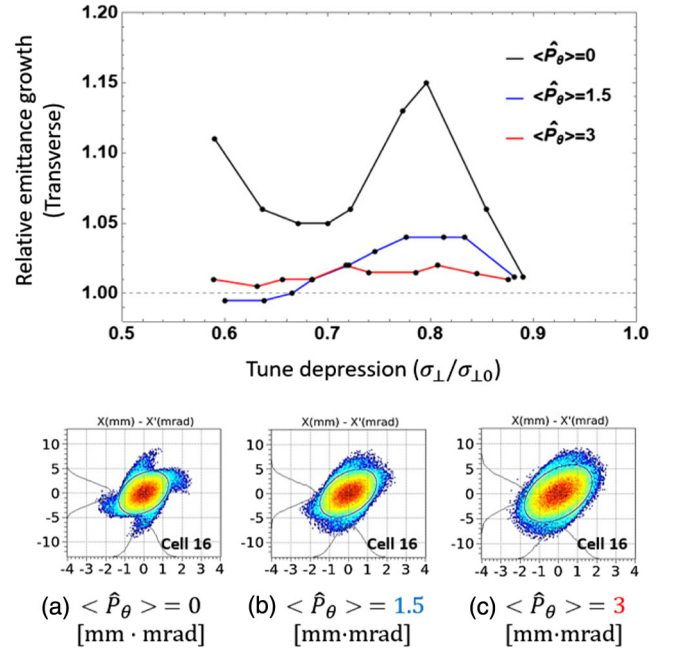


FIG. 4. Relative emittance growth over 20 periods along the solenoid focusing lattice for $\sigma_{\perp 0} = 100^\circ$ without acceleration. Emittance growth results mainly from the fourth-order particle resonance. The phase-space plots for cell 16 are shown for the (a) $\langle \hat{P}_\theta \rangle = 0$, (b) $\langle \hat{P}_\theta \rangle = 1.5$, and (c) $\langle \hat{P}_\theta \rangle = 3$ mm mrad beams for a tune depression of $\sigma_\perp/\sigma_{\perp 0} = 0.8$. The maximum relative emittance growth is reduced from 15% to 2% for the spinning beams. The fourth-order particle resonance is mitigated with fewer particles populating the fourfold structures of the spinning beams.

the transverse and longitudinal planes. The initial normalized transverse rms emittance for the nonspinning beam is $\epsilon_{N_{rms,\perp}} = 0.1 \text{ mm} \cdot \text{mrad}$, and the longitudinal rms emittance is $\epsilon_{N_{rms,z}} = 0.3 \text{ mm} \cdot \text{mrad}$ (or, equivalently, $0.06 \text{ deg} \cdot \text{MeV}$). The initial normalized rms emittances for the spinning beams are $\epsilon_{N_{rms,\perp}} = 0.132 \text{ mm} \cdot \text{mrad}$ and $\epsilon_{N_{rms,z}} = 0.3 \text{ mm} \cdot \text{mrad}$ for the $\langle \hat{P}_\theta \rangle = 1.5 \text{ mm} \cdot \text{mrad}$ beam and $\epsilon_{N_{rms,\perp}} = 0.188 \text{ mm} \cdot \text{mrad}$ and $\epsilon_{N_{rms,z}} = 0.3 \text{ mm} \cdot \text{mrad}$ for the $\langle \hat{P}_\theta \rangle = 3 \text{ mm} \cdot \text{mrad}$ beam. The required field of a solenoid magnet is 0.5 T for generating a $\langle \hat{P}_\theta \rangle = 1.5 \text{ mm} \cdot \text{mrad}$ beam and 1 T for generating a $\langle \hat{P}_\theta \rangle = 3 \text{ mm} \cdot \text{mrad}$ beam in the simulation.

As shown in Fig. 4, the maximum relative emittance growth from the fourth-order resonance is 15% for the nonspinning beam (black line) at $\sigma_\perp/\sigma_{\perp 0} = 0.8$. On the other hand, for the spinning beam with $\langle \hat{P}_\theta \rangle = 3 \text{ mm} \cdot \text{mrad}$, it is only 2% (red line). As $\langle \hat{P}_\theta \rangle$ increases, the values of the emittance growth over the tune depression space become more or less constant. The phase-space plots at cell 16 for the nonspinning and spinning beams are shown for $\sigma_\perp/\sigma_{\perp 0} = 0.8$. It is clearly observed that the fourth-order particle resonance is mitigated with fewer particles populating the fourfold structures in Figs. 4(b) and 4(c) compared with those in Fig. 4(a).

Figure 5 shows the relative emittance growth over ten periods and the phase-space plots under the quadrupole-doublet focusing lattice without acceleration. The beam parameters are the same as those for Fig. 4. For a quadrupole-doublet focusing lattice, the beam is not axisymmetric; thus, the relative emittance growth is calculated by taking the average of the emittance growth values in the x and y planes. The phase-space plots at cell 10 for the nonspinning and spinning beams are shown for $\sigma_\perp/\sigma_{\perp 0} = 0.82$. As the initial $\langle \hat{P}_\theta \rangle$ increases, the maximum average relative emittance growth decreases from 30% to 14%, and the population of particles within the fourfold structures is reduced for spinning beams. Because the average canonical angular momentum is not conserved under the quadrupole lattice, the beam spinning effects on the fourth-order resonance vary across the periods. In this sense, the suppression of the fourfold structures shown in Figs. 5(b) and 5(c) is less apparent than of those in Figs. 4(b) and 4(c).

As discussed in Ref. [14], it should be emphasized that the spinning effect is evidently different from the case of increasing thermal emittance only. If the initial rms emittance of the nonspinning beam is set equal to that of the spinning beam by merely increasing the thermal emittance, there is no mitigation impact in the absence of spinning.

In our multiparticle simulations with acceleration, which will be discussed in the next section, the initial rms emittances and beam sizes of nonspinning beams are set

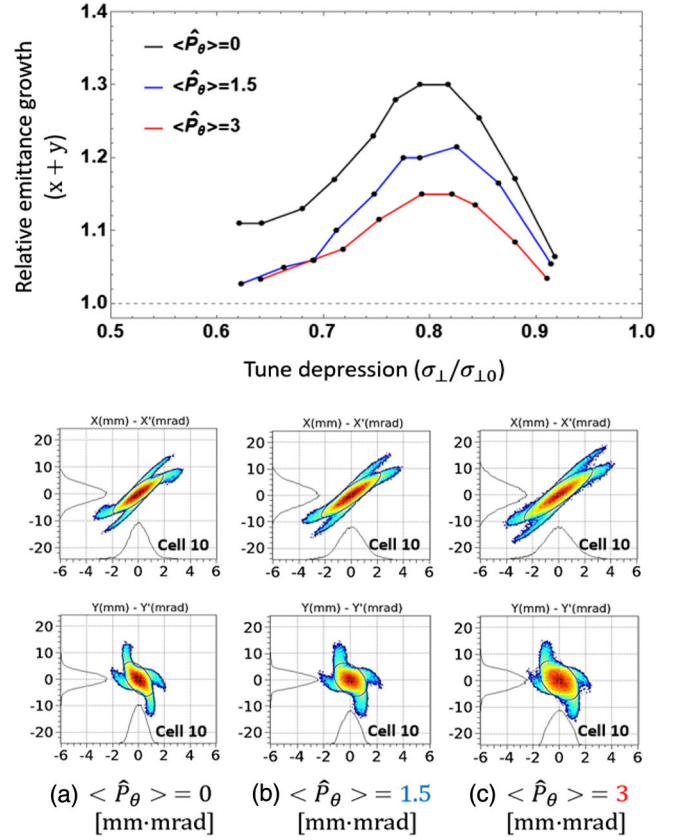


FIG. 5. Relative emittance growth over ten periods along the quadrupole focusing lattice for $\sigma_{\perp 0} = 100^\circ$ without acceleration. Emittance growth results mainly from the fourth-order particle resonance. The phase-space plots at cell 10 are shown for (a) $\langle \hat{P}_\theta \rangle = 0$, (b) $\langle \hat{P}_\theta \rangle = 1.5$, and (c) $\langle \hat{P}_\theta \rangle = 3 \text{ mm mrad}$ beams for a tune depression of $\sigma_\perp/\sigma_{\perp 0} = 0.82$. The maximum average relative emittance growth decreases from 30% to 14% for the spinning beams. The suppression of the fourfold structures in (b) and (c) is less apparent than of those in Figs. 4(b) and 4(c), because the average canonical angular momentum is not conserved under the quadrupole lattice.

the same as those of spinning beams. Because angular momentum increases rms emittances, we use the same rms emittances for nonspinning beams for a proper comparison.

B. Spinning effects with acceleration

As discussed in the previous section, for $\sigma_{\perp 0} > 90^\circ$, both the envelope instability and fourth-order particle resonance are important sources of halo evolution. Therefore, we must avoid the stop bands or mitigate the excitation of the instability and resonance. We confirmed that the fourth-order particle resonance can be mitigated by beam spinning even for the 3D bunched beam cases.

In Ref. [19], Qiang reported that envelope instability can be mitigated with a high accelerating gradient in a

periodic solenoid (or quadrupole) and rf focusing channels in high-intensity linacs. If zero-current phase advance is to be constant, the depressed phase advance increases as beam accelerates, passing through the envelope instability stop band.

Figure 6 shows the transverse phase advances, relative emittance growth, and halo parameter for cases with and without acceleration under the solenoid focusing lattice. The zero-current phase advance is maintained to be constant for $\sigma_{\perp 0} = 100^\circ$ over 100 lattice periods. Here, the halo parameter H_i (i for x , y , and z) is defined as the ratio between the fourth-order and second-order moments of the beam in 2D phase space (q_i, p_i) [32]:

$$H_i \equiv \frac{\sqrt{3\langle q_i^4 \rangle \langle p_i^4 \rangle + 9\langle q_i^2 p_i^2 \rangle^2 - 12\langle q_i p_i^3 \rangle \langle q_i^3 p_i \rangle}}{2\langle q_i^2 \rangle \langle p_i^2 \rangle - 2\langle q_i p_i \rangle^2} - 2. \quad (6)$$

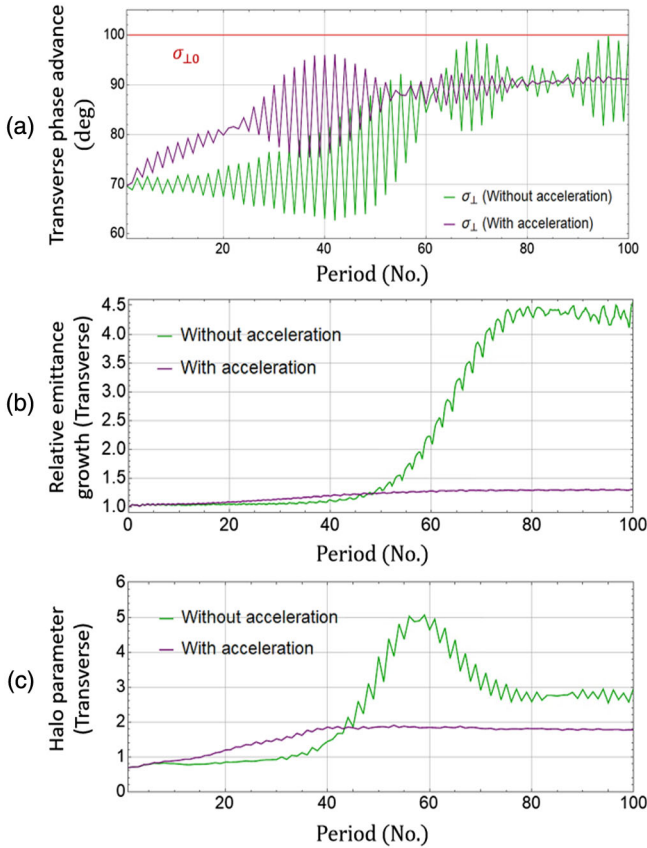


FIG. 6. (a) Transverse phase advances, (b) relative emittance growth, and (c) halo parameter for cases with and without acceleration under the solenoid focusing lattice. The transverse zero-current phase advance is maintained to be constant for $\sigma_{\perp 0} = 100^\circ$ over 100 periods. Envelope instability can be mitigated with a high accelerating gradient (purple lines), which leads to passing through the envelope instability stop band faster than beams without acceleration (green lines). Here, the accelerating gradient is 5 MV/m, and the beam current is 10 mA.

For uniform Kapchinskij-Vladimirskij (K-V) distribution, $H_i = 0$, and for the Gaussian distribution, $H_i = 1$. A significant halo population in the multiparticle simulations corresponds to $H_i > 1$.

Without acceleration (green lines in Fig. 6), the beam remains within the fourth-order particle resonance stop band over 40 periods and generates an envelope mismatch, which accordingly induces a large emittance growth over around 50–80 periods within the envelope instability stop band [20].

When there is an accelerating rf field (purple lines in Fig. 6), the depressed phase advance increases as the beam is accelerated, because the space charge effect scales as $1/\beta^2\gamma^3$ [see Eqs. (1) and (2)]. This causes the beam to pass through the envelope instability stop band faster than a beam without acceleration. Therefore, the beam does not have sufficient time to evolve envelope instability, and the corresponding emittance growth and halo parameter do not significantly increase over 100 periods [19]. Here, the accelerating rf gradient is 5 MV/m, and the beam current is 10 mA. We assume that the initial beam has well-matched Gaussian profiles in both the transverse and longitudinal planes.

By applying a fast acceleration, it is confirmed that we can suppress the envelope instability observed after long lattice periods in linacs. Even in this situation, the fourth-order particle resonance is manifested within 5–40 lattice periods and can still be an important source for emittance growth and halo formation. In this sense, the mitigation effect of beam spinning on the fourth-order resonance is more important when beams are accelerated along linacs, which will be further discussed below.

Figure 7 shows the spinning effects on the fourth-order particle resonance in the transverse plane, while the beams are accelerated from 5 to 18 MeV over 40 periods under the solenoid focusing lattice. The accelerating voltages of cavities are $0.3 \text{ MV} < V_{\text{acc}} < 0.5 \text{ MV}$. The transverse zero-current phase advance decreases from 120° to 90° as the beams are accelerated, and the depressed phase advance stays constant around $\sigma_{\perp} \sim 76^\circ$ along the linac, which causes the beam to remain within the fourth-order resonance stop band [see Fig. 7(a)]. The initial longitudinal phase advance is $\sigma_{z0} = 30^\circ$, whereby there is no emittance exchange between the transverse and longitudinal spaces. It should be emphasized again that, for simulation studies with acceleration, the initial normalized rms emittances and rms beam sizes of the spinning and nonspinning beams are the same. The initial beam parameters are summarized in Fig. 7(d).

If we operate accelerators with $\sigma_{\perp 0} > 90^\circ$, which means that the external focusing can be further increased, we could make the initial beam size almost the same as the case of $\sigma_{\perp 0} < 90^\circ$, even with much higher beam currents (see Appendix A for an analytical description). In this case, nevertheless, we should handle the excitation of incoherent

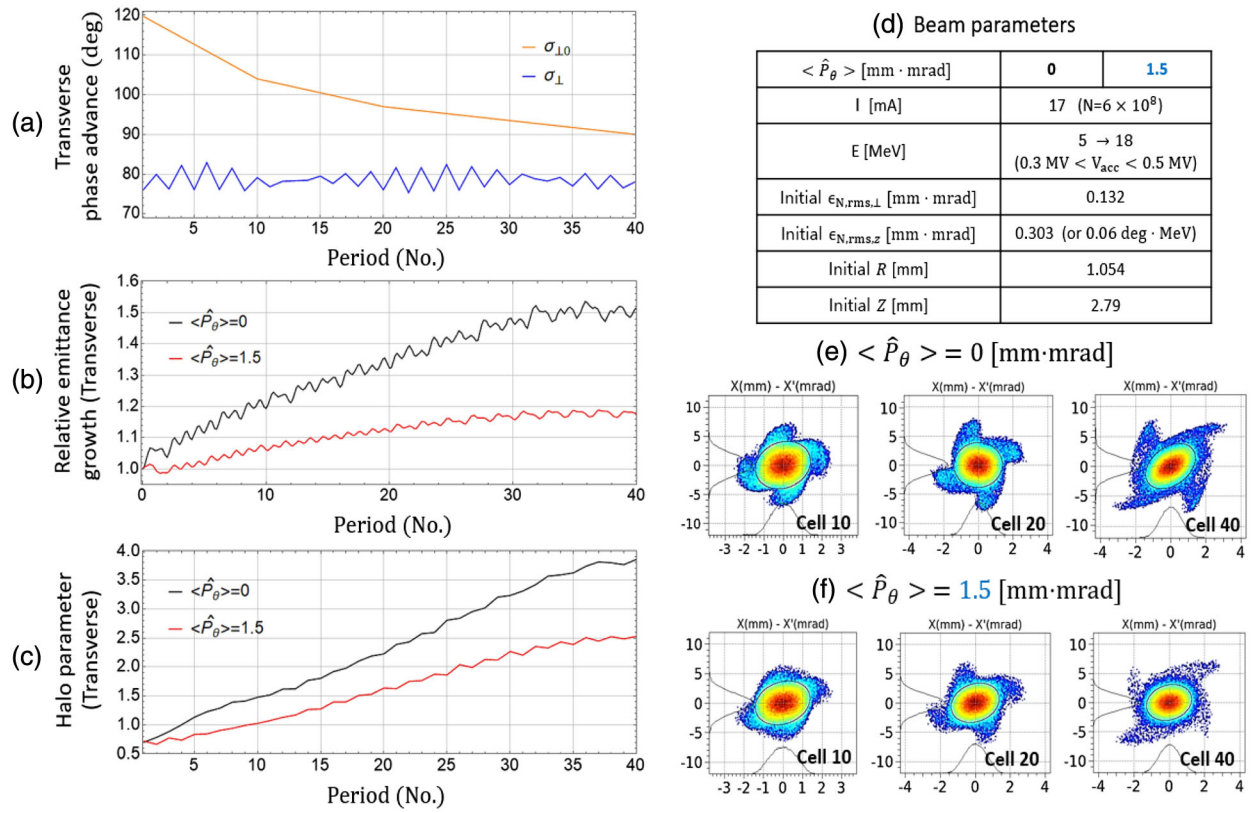


FIG. 7. (a) Transverse phase advances, (b) relative emittance growth, and (c) halo parameter of the nonspinning and spinning beams under the solenoid focusing lattice. Here, $\sigma_{\perp 0}$ decreases from 120° to 90° (yellow line) as the beams are accelerated from 5 to 18 MeV over 40 periods. The depressed phase advance remains constant around $\sigma_{\perp} \sim 76^\circ$ along the linac (blue line), which is within the fourth-order resonance stop band. (d) The initial beam parameters for nonspinning and spinning beams are the same. Phase-space plots are shown for the (e) $\langle \hat{P}_\theta \rangle = 0$ and (f) $\langle \hat{P}_\theta \rangle = 1.5$ mm mrad beams. For the spinning beam, the population of particles in the four resonance islands is reduced, and the associated emittance growth and halo parameter evidently decrease (red lines). The initial longitudinal phase advance is $\sigma_{z0} = 30^\circ$, whereby there is no emittance exchange between the transverse and longitudinal spaces.

particle resonances along the beam propagation (suppose that the envelope instability is already managed by the fast acceleration). If we can allow the increase of the final rms emittances within a certain acceptable range, then we may generate and apply spinning beams to suppress the halo formations associated with the fourth-order resonance. For very high-intensity accelerators operating near the space-charge-dominated regime, rather than the rms emittance itself, the halo suppressions are much more critical in controlling beam sizes and losses [33]. Furthermore, we note the main applications of the spinning beam we have in mind are high-intensity linacs that are directly coupled to targets, not for ring injections. Hence, the final rms emittance requirement might not be so tight. Of course, identifying the parameter space in which beam spinning might be beneficial for actual high-intensity linac operations should involve more dedicated parametric studies. An example of such parametric studies for spinning beams under fast acceleration is given in Appendix B.

As shown in Fig. 7(e), fourth-order resonance is manifested after short periods, and fourfold structures

are clearly observed at cells 10, 20, and 40 in the phase-space plots. The relative emittance increases up to 50%, and the halo parameter increases from 0.7 to 3.9 over 40 periods [black lines in Figs. 7(b) and 7(c)]. For the spinning beam shown in Fig. 7(f), the population of particles in the four resonance islands is reduced, the associated maximum emittance growth is 20%, and the halo parameter increases from 0.7 to 2.5 [red lines in Figs. 7(b) and 7(c)]. It is demonstrated that the mitigation effect of beam spinning on fourth-order resonance is evidently observed in terms of lower emittance growth and halo parameter.

The spinning effects on fourth-order resonance under the quadrupole focusing lattice are shown in Fig. 8. The transverse zero-current phase advance decreases from 110° to 88° as the beam is accelerated from 5 to 12.4 MeV. The depressed phase advance remains constant around $\sigma_{\perp} \sim 76^\circ$ along the linac, which causes the beam to remain within the fourth-order resonance stop band [see Fig. 8(a)]. The beam parameters of both nonspinning and spinning beams are summarized in Fig. 8(d). For the spinning beam, shown in

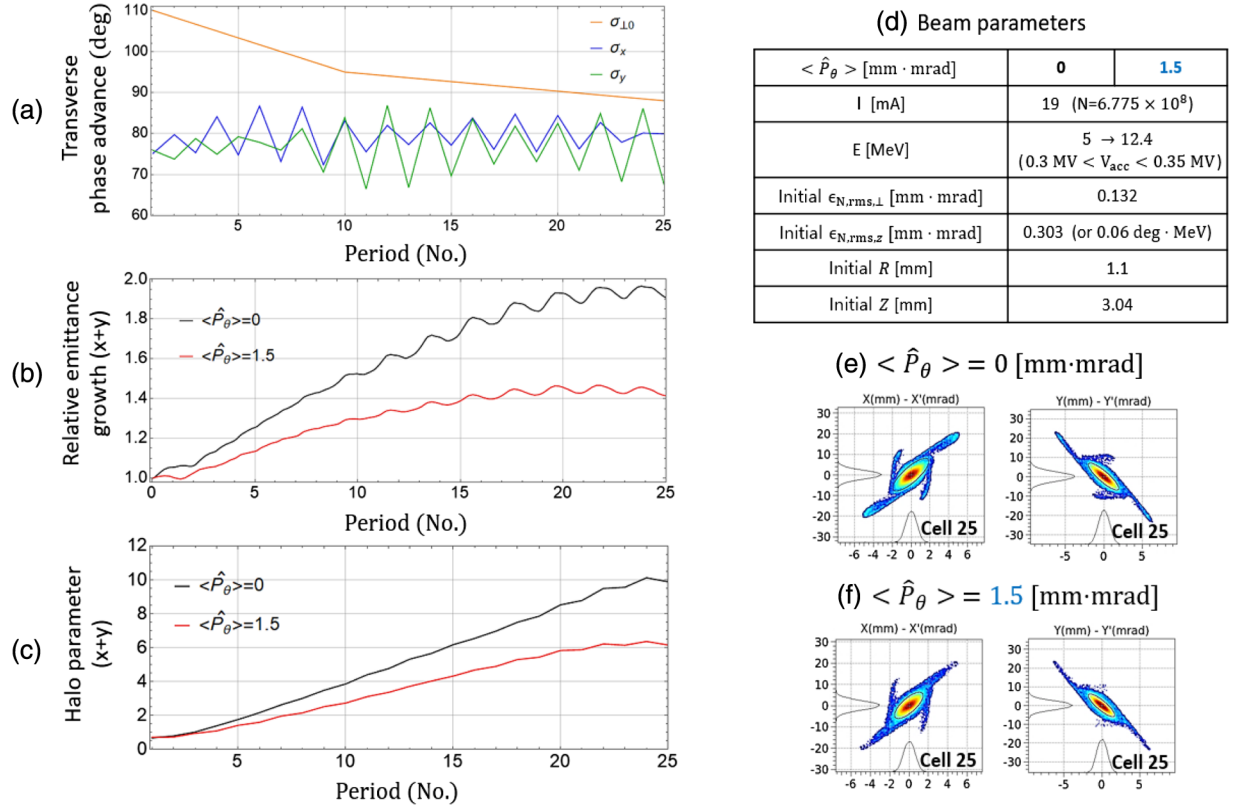


FIG. 8. (a) Transverse phase advances, (b) relative emittance growth, and (c) halo parameter of the nonspinning and spinning beams under the quadrupole focusing lattice. Here, $\sigma_{\perp 0}$ decreases from 110° to 88° (yellow line) as the beams are accelerated from 5 to 12.4 MeV over 25 periods. The depressed phase advance remains constant around $\sigma_{\perp} \sim 76^\circ$ along the linac (blue and green lines), which is within the fourth-order resonance stop band. (d) The initial beam parameters for nonspinning and spinning beams are the same. Phase-space plots are shown for the (e) $\langle \hat{P}_\theta \rangle = 0$ and (f) $\langle \hat{P}_\theta \rangle = 1.5$ mm mrad beams. For the spinning beam, the population of particles in the four resonance islands is reduced, and the associated emittance growth and halo parameter evidently decrease (red lines). The initial longitudinal phase advance is $\sigma_{z0} = 30^\circ$, whereby there is no emittance exchange between the transverse and longitudinal spaces.

Fig. 8(f), the population of particles in the four resonance islands in both the x and y phase spaces is reduced. In addition, for the spinning beam, the maximum emittance growth decreases from 95% to 45%, and the maximum average halo parameter decreases from 10 to 6 [see Figs. 8(b) and 8(c)]. Even though average canonical angular momentum is not conserved under the quadrupole lattice, the beam spinning effects on fourth-order resonance are still valid.

So far, we have investigated whether the fourth-order particle resonance in the transverse space can be mitigated by beam spinning when $\sigma_{\perp 0} > 90^\circ$ and $\sigma_{\perp} < 90^\circ$ during beam acceleration under the solenoid and quadrupole focusing channels. It has been illustrated by multiparticle simulations that the relative emittance growths and halo parameters are indeed reduced owing to the mitigation of the fourth-order resonance driving effect, which is associated with nonzero canonical angular momentum.

In the next section, we deal with the longitudinal beam dynamics for $\sigma_{z0} > 90^\circ$ and with possible beam spinning effects in longitudinal space.

IV. FOURTH-ORDER PARTICLE RESONANCE IN LONGITUDINAL SPACE

In recent studies in Refs. [34,35] for lattice structures with more than one rf gap per external focusing period, it was reported that the 90° restriction need not be applied to the longitudinal space in the same way as to the transverse one. However, for periodic lattices in which the transverse focusing and rf gap have the same lattice period as in Figs. 1 and 2, we expect fourth-order particle resonance to occur in longitudinal space under the conditions of $\sigma_{z0} > 90^\circ$ and $\sigma_z < 90^\circ$, similar to the transverse case. Here, $\sigma_{z0}(\sigma_z)$ is the longitudinal zero-current (depressed) phase advance per lattice period.

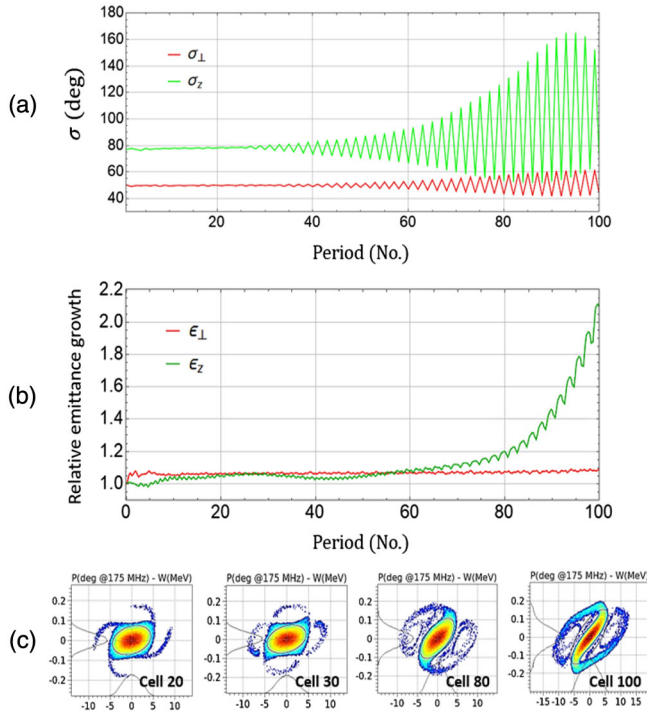


FIG. 9. (a) Depressed phase advances and (b) relative emittance growth under the solenoid focusing lattice without acceleration. The longitudinal phase advances are $\sigma_{z0} = 100^\circ$ and $\sigma_z = 77^\circ$, at which the beam remains within the fourth-order particle resonance stop band. Fourth-order resonance is predominantly manifested over 40 periods, drawing four separate islands on (c) the phase (deg) vs energy (MeV) planes. Envelope instability occurs as σ_z increases to over 90° , accompanied by large emittance growth (green lines).

First, multiparticle simulations are performed to explore the fourth-order particle resonance in the longitudinal plane without acceleration. Figure 9 shows the depressed phase advances and relative emittance growth over 100 periods under the solenoid focusing lattice without acceleration. Here, the initial longitudinal phase advances are set to $\sigma_{z0} = 100^\circ$ and $\sigma_z = 77^\circ$. Such parameters transform the beam into a fourth-order resonance in longitudinal space. The initial transverse phase advances are $\sigma_{\perp 0} = 85^\circ$ and $\sigma_{\perp} = 50^\circ$, where there is no coupling effect between the transverse and longitudinal spaces. The beam energy is 5 MeV, and the beam current is 14.5 mA. The longitudinal depressed phase advance remains constant over 40 periods, and the fourth-order resonance is predominantly manifested by drawing four separate islands in the phase (deg)-energy (MeV) planes at cells 20 and 30 in Fig. 9(c). Subsequently, the beam becomes unstable, and the beam mismatch induces envelope instability as σ_z increases to over 90° . Similar to the transverse dynamics, envelope instability in longitudinal space occurs following the fourth-order resonance with a large emittance growth (green lines).

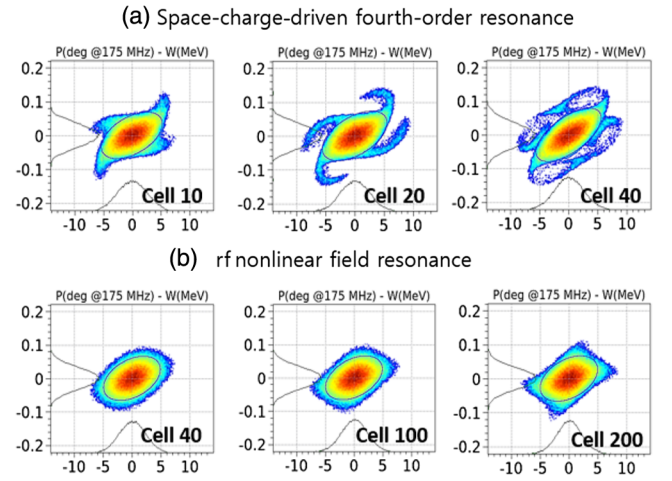


FIG. 10. The fourth-order resonances generated from a (a) nonlinear space charge field and (b) rf nonlinear field. In (a), the space-charge-driven fourth-order resonance occurs from cell 10, and resonance islands are clearly observed in the phase plane. In (b), the rf nonlinear field resonance is much weaker and begins to appear after cell 100.

When the longitudinal zero-current phase advance is greater than 90° , the nonlinear fields of the rf cavities can excite nonlinear resonances in addition to space-charge-driven particle resonances [27,36]. Nevertheless, for our multiparticle simulations, the rf nonlinear resonances can be neglected, because they develop very slowly and occur only when the longitudinal beam size is much larger than the range considered in this study (see Fig. 10). In Fig. 10(a), the space-charge-driven fourth-order particle resonance is clearly observed in cell 10, drawing four separate islands in the phase plane. By contrast, as shown in Fig. 10(b), the resonance structures generated from the rf nonlinear fields are observed to be much weaker and appear after cell 100.

Now, we investigate the beam spinning effects in the longitudinal plane. Figure 11 shows the longitudinal phase advances, relative emittance growth, halo parameter, beam parameters, and the phase-space plots for the $\langle \hat{P}_\theta \rangle = 0$ and $\langle \hat{P}_\theta \rangle = 1.5 \text{ mm} \cdot \text{mrad}$ beams. The beams are accelerated from 5 to 20 MeV over 20 periods under a solenoid focusing lattice. As the beam is accelerated, the longitudinal zero-current phase advance decreases from 120° to 90° , whereas the depressed phase advance remains constant around $\sigma_z \sim 75^\circ$. Hence, the beam remains within the fourth-order resonance stop band. There is no emittance exchange between the transverse and longitudinal planes; thus, the nonzero average canonical angular momentum around the beam propagation axis does not affect the longitudinal distributions. As shown in Figs. 11(b) and 11(c), the relative emittance growth and halo parameters do not reveal significant differences between the nonspinning and spinning beams. The resonance structures on the phase

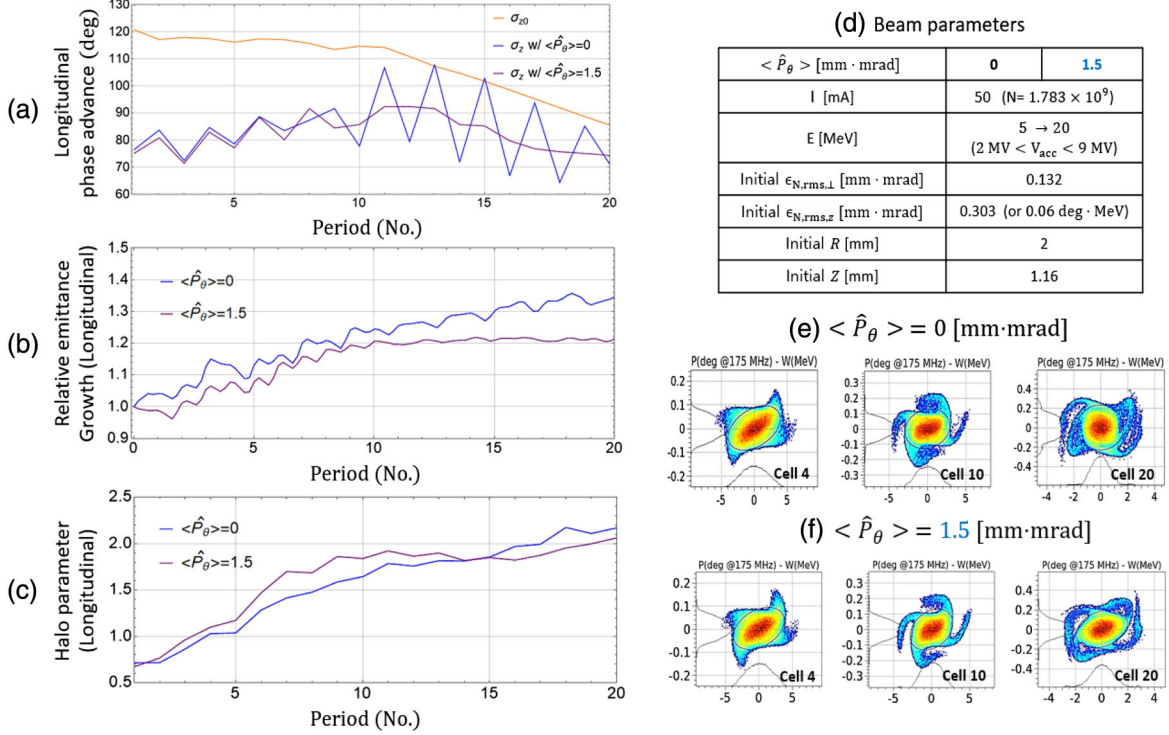


FIG. 11. (a) Longitudinal phase advances, (b) relative emittance growth, (c) halo parameter, and (d) beam parameters under the solenoid focusing lattice. Here, σ_{z0} decreases from 120° to 90° as the beams are accelerated from 5 to 20 MeV over 20 periods. (e) and (f) show the phase (deg) · energy (MeV) plots of nonspinning and spinning beams, respectively. The resonance structures are clearly shown in both (e) and (f) to be independent of the canonical angular momentum of the beam. The initial transverse phase advances are $\sigma_{\perp 0} = 85^\circ$ and $\sigma_{\perp 1} = 50^\circ$, whereby there is no emittance exchange between the transverse and longitudinal spaces.

(deg) · energy (MeV) planes are clearly shown in both Figs. 11(e) and 11(f) to be independent of the canonical angular momentum of the beam.

V. SUMMARY AND DISCUSSIONS

Recently, understanding space-charge-driven incoherent particle resonances in high-intensity linear accelerators has become increasingly important. For Gaussian density beams, fourth-order particle resonance is dominantly observed over short periods, and its stop band is wider than the envelope instability stop band. For designing new high-intensity linacs, overcoming the 90° phase advance limit is highly desirable in order to expand the choice of accelerator parameters, including beam currents and external focusing fields. By applying fast acceleration, the envelope instability could be bypassed, although fourth-order particle resonance still remains an important source of beam degradation.

In this regard, we propose a possible mitigation for fourth-order particle resonance in high-intensity linacs by applying beam spinning. We performed a detailed investigation of the beam spinning effects for 3D bunched beams under the solenoid and quadrupole-doublet focusing lattices. We numerically observed that beam spinning could mitigate fourth-order resonance in transverse space and,

accordingly, suppress emittance growth and halo formation. Also, it was verified that the intrinsic characteristic of the spinning beam on the particle resonance comes from nonzero average canonical angular momentum, not from a thermal emittance increase in the absence of spinning.

Furthermore, for $\sigma_{z0} > 90^\circ$ and $\sigma_z < 90^\circ$, we found that fourth-order particle resonance could be triggered in the longitudinal plane. For high-intensity linacs, we expect the space-charge-driven longitudinal resonances to be dominant over rf nonlinear field effects. Spinning effects were not clearly observed for longitudinal fourth-order resonance compared with their mitigation effects on the transverse plane.

The halo parameter defined in Eq. (6) provides information about beam distribution in terms of spatial and momentum coordinates of the particles. Through our simulations, we used this halo parameter as a figure of merit, because it is most commonly chosen for the analysis of halo formations and beam losses. Nevertheless, the precise definition of halo and core limit was not available here, and the halo parameter has no information about the location or the extent of halos. More advanced figures of merit could be adopted in the future. For example, Nghiem *et al.* reported [37,38] new halo definitions, which characterize the beam halo by the percentage of halo size and halo particles.

A rotating ion beam could be generated either by using a magnetized ion source or by stripping an ion beam inside a solenoid [23]. We propose the stripping of H^- (or D^-) beams inside a pair of solenoids installed in a medium-energy beam transport line and injecting the resultant spinning H^+ (or D^+) beams into the main linac after proper matching [14]. The solenoid magnetic field necessary for generating spinning beams for our simulation studies is approximately 1–2 T, which is within the practical experimental range. Nevertheless, there would remain several technical issues to be addressed to apply the spinning beams in actual linacs. For example, we should minimize particle loss and emittance growth during the stripping process, and we also may need to remove the correlation in the transverse plane at the end of the linac to match the footprint requirement on the target.

Even if $\sigma_0 < 90^\circ$ (i.e., with neither fourth-order resonance nor envelope instability), spinning beams could be applied to reduce beam losses from initial mismatches and machine imperfections, motivated by the mechanical stability principle of spinning flying objects [14]. This feature is under investigation and will be reported elsewhere. As pointed out in a recent paper [39], rather than angular momentum, integrated beam vorticity is a more general and fundamental beam property that yields difference in eigenemittances. In this regard, what exact beam property (angular momentum, difference in eigenemittances, or beam vorticity) mitigates fourth-order particle resonance would be an important question to be addressed to optimize the mitigation process. We believe that spinning beam studies can give a rich and promising research direction for mitigating incoherent particle resonances and achieving much higher-intensity linear accelerators in the future.

ACKNOWLEDGMENTS

This study was supported by the National Research Foundation (NRF) of Korea (Grants No. NRF-2019R1A2C1004862 and No. NRF-2020R1A2C1010835). This work was also supported by the Rare Isotope Science Project of the Institute for Basic Science, funded by the Ministry of Science and ICT (MSIT) and the NRF of Korea under Contract No. 2013M7A1A1075764.

APPENDIX A: BEAM PARAMETER SCALING WITH CANONICAL ANGULAR MOMENTUM

Within the smooth-focusing approximation, the transverse beam size r_b at the matched condition is given by the following algebraic equation [24]:

$$\kappa_{sf} r_b - \frac{K}{r_b} - \frac{\epsilon_T^2}{r_b^3} = 0, \quad (\text{A1})$$

where κ_{sf} is a constant lattice coefficient that describes the average effect of periodic quadrupole or solenoidal fields

and ϵ_T indicates the rms edge emittance. In the presence of canonical angular momentum,

$$\epsilon_T = 4\sqrt{\epsilon_{th,\perp}^2 + \langle \hat{P}_\theta \rangle^2 / 4} = \epsilon_{T,0} \sqrt{1 + \eta^2}, \quad (\text{A2})$$

where $\eta = \langle \hat{P}_\theta \rangle / 2\epsilon_{th,\perp}$ and $\epsilon_T = 4\epsilon_{th,\perp} = \epsilon_{T,0}$ for $\eta = 0$. The general solution of Eq. (A1) can be written in the following form:

$$r_b = a_B \left(\frac{1}{2} + \frac{1}{2} \sqrt{1 + u^{-2}} \right)^{1/2}. \quad (\text{A3})$$

Here, $a_B = \sqrt{K/\kappa_{sf}}$ is the beam radius of the Brillouin flow, and u is a dimensionless parameter defined by [24]

$$u = \frac{K}{2\epsilon_T \sqrt{\kappa_{sf}}}. \quad (\text{A4})$$

Now, suppose that we want to increase the beam current while keeping the matched beam radius constant. This can be done by increasing the focusing strength with allowing some emittance increase. For example, if the increases of the focusing strength and emittance vary as follows:

$$\frac{\kappa_{sf}}{\kappa_{sf,0}} = 1 + \eta^2, \quad (\text{A5})$$

$$\frac{\epsilon_T}{\epsilon_{T,0}} = \sqrt{1 + \eta^2}, \quad (\text{A6})$$

then we would have the following scalings:

$$\frac{K}{K_0} = 1 + \eta^2, \quad (\text{A7})$$

$$\frac{\sigma_{\perp 0}}{\sigma_{\perp 0,0}} = \sqrt{1 + \eta^2}. \quad (\text{A8})$$

Here, the subscript 0 denotes the value at $\eta = 0$, and $\sigma_{\perp 0}$ is the transverse zero-current phase advance.

We note that, for a desired matched beam radius, we could accommodate much higher beam currents by applying such scalings. In practice, however, we cannot indefinitely increase the focusing strength mainly because of the $\sigma_{\perp 0} = 90^\circ$ limit. In the operation range of $\sigma_{\perp 0} < 90^\circ$, there might not be much benefit of beam spinning. In this case, there is no resonance mitigation effect by the beam spinning, and it simply increases the total emittance.

If we go beyond the $\sigma_{\perp 0} = 90^\circ$ limit, the beam spinning could mitigate fourth-order particle resonance and may allow stable beam transport with much higher beam currents. Nevertheless, from the stability requirement of

single-particle motion in a periodic focusing channel, we should have at least $\sigma_{\perp 0} < 180^\circ$ [36]. Hence, the parameter space in which the beam spinning might be of any advantage would be

$$90^\circ < \sigma_{\perp 0,0} \sqrt{1 + \eta^2} < 180^\circ. \quad (\text{A9})$$

A (conservative) upper limit for η could be obtained by setting $\sigma_{\perp 0,0} \rightarrow 90^\circ$ as

$$\eta = \frac{\langle \hat{P}_\theta \rangle}{2\epsilon_{\text{th},\perp}} < \sqrt{3}. \quad (\text{A10})$$

Certainly, searching for parameter space in which beam spinning might be effective for actual high-intensity linacs should involve more elaborate case studies in terms of numerical simulations. Nonetheless, the basic beam parameter scalings for the matched beam radius, focusing strength, emittance, perveance, and phase advance introduced here in the presence of canonical angular momentum will be useful for guiding such parametric studies.

APPENDIX B: AN EXAMPLE OF A PARAMETRIC STUDY FOR THE SPINNING BEAM

In Fig. 12, we illustrate an example of a parametric study for the spinning beam. The beam current, rms beam size, normalized rms emittance, and halo parameter are plotted as a function of $\langle \hat{P}_\theta \rangle$ when the beams are accelerated from 5 to 18.5 MeV. Here, $\sigma_{\perp 0}$ decreases from 120° to 90° as the beams are accelerated, and $\sigma_{\perp} \sim 76^\circ$ remains constant along the linac. The final beam parameters (as denoted by red lines) are calculated after 40 lattice periods of the solenoid focusing channel.

With nonzero canonical angular momentum, the initial rms emittances increase as expressed in Eq. (A2). Figure 12(c) shows the initial and final normalized rms emittances as $\langle \hat{P}_\theta \rangle$ increases. For $\langle \hat{P}_\theta \rangle \leq 1.05 \text{ mm} \cdot \text{mrad}$, the final rms emittances are smaller than that of the nonspinning beam, which suggests the mitigation effects of the spinning beams are stronger than the rate of the initial emittance increase. On the other hand, for $\langle \hat{P}_\theta \rangle > 1.05 \text{ mm} \cdot \text{mrad}$, the final rms emittances are larger than that of the nonspinning beam, because the initial rms emittance growths are too high. However, it should be emphasized that the relative emittance growth (i.e., the ratio

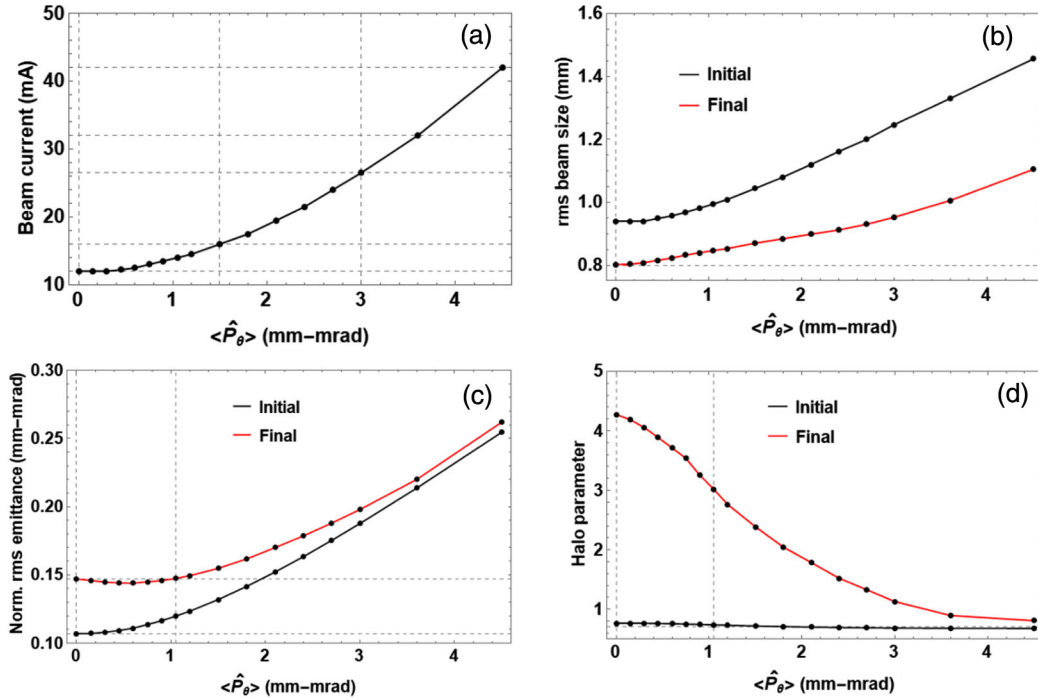


FIG. 12. A parametric study with various values of $\langle \hat{P}_\theta \rangle$. (a) Beam current (mA), (b) rms beam size (mm), (c) normalized rms emittance (mm · mrad), and (d) halo parameter with acceleration under the solenoid focusing lattice. Here, $\sigma_{\perp 0}$ decreases from 120° to 90° as the beams are accelerated, and $\sigma_{\perp} \sim 76^\circ$ remains constant along the linac. For the same tune depression space, the beam current could be increased as $\langle \hat{P}_\theta \rangle$ increases. For the spinning beams, the initial emittance increases from canonical angular momentum, but the relative emittance growth [i.e., the ratio of final emittance to initial emittance in (c)] is substantially reduced. The mitigation effect of the spinning beam on fourth-order particle resonance is evidently observed in terms of the suppression of the halo parameters [red line in (d)].

of final emittance to initial emittance) decreases as $\langle \hat{P}_\theta \rangle$ increases, mainly because the fourth-order particle resonance is mitigated by the spinning effects.

In our study, the main point for applying spinning beams is to mitigate halo formations associated with fourth-order particle resonance at the expense of some increase in the final rms emittance. As shown in Fig. 12(d), the mitigation effects of spinning beams on fourth-order particle resonance are evidently observed in terms of the suppression of the halo parameters (red line).

For the same tune depression range along the linac, the beam currents of the spinning beams can be made much larger compared to the nonspinning beam case [see Fig. 12(a)]. This illustrates a merit of overcoming the 90° limit for higher-intensity linac operations. In this particular example, the initial rms beam sizes are allowed to increase according to the value of $\langle \hat{P}_\theta \rangle$, whereas the final rms beam sizes are reduced from the initial ones after the acceleration [see Fig. 12(b)].

-
- [1] M. Tiefenback and D. Keefe, *IEEE Trans. Nucl. Sci.* **32**, 2483 (1985).
- [2] D. Jeon, L. Groening, and G. Franchetti, *Phys. Rev. Accel. Beams* **12**, 054204 (2009).
- [3] L. Groening, W. Barth, W. Bayer, G. Clemente, L. Dahl, P. Forck, P. Gerhard, I. Hofmann, M. Kaiser, M. Maier *et al.*, *Phys. Rev. Lett.* **102**, 234801 (2009).
- [4] D.-O. Jeon, *Phys. Rev. Accel. Beams* **19**, 010101 (2016).
- [5] D. Jeon, J. Jang, and H. Jin, *Nucl. Instrum. Methods Phys. Res., Sect. A* **832**, 43 (2016).
- [6] D. Jeon and K. R. Hwang, *Phys. Plasmas* **24**, 063108 (2017).
- [7] D.-O. Jeon, *J. Korean Phys. Soc.* **72**, 1523 (2018).
- [8] I. Hofmann, A. Oeftiger, and O. Boine-Frankenheim, *Phys. Rev. Accel. Beams* **24**, 024201 (2021).
- [9] I. Hofmann, L. J. Laslett, L. Smith, and I. Haber, *Part. Accel.* **13**, 145 (1982).
- [10] C. Chen and R. C. Davidson, *Phys. Rev. Lett.* **72**, 2195 (1994).
- [11] S. M. Lund and B. Bukh, *Phys. Rev. Accel. Beams* **7**, 024801 (2004).
- [12] C. Li and Q. Qin, *Phys. Plasmas* **22**, 023108 (2015).
- [13] J. Qiang, *Phys. Rev. Accel. Beams* **21**, 034201 (2018).
- [14] Y.-L. Cheon, S.-H. Moon, M. Chung, and D.-O. Jeon, *Nucl. Instrum. Methods Phys. Res., Sect. A* **1013**, 165647 (2021).
- [15] Y.-E. Sun, P. Piot, K.-J. Kim, N. Barov, S. Lidia, J. Santucci, R. Tikhoplav, and J. Wennerberg, *Phys. Rev. Accel. Beams* **7**, 123501 (2004).
- [16] K.-J. Kim, *Phys. Rev. Accel. Beams* **6**, 104002 (2003).
- [17] A. Burov, S. Nagaitsev, and A. Shemyakin, *Phys. Rev. Accel. Beams* **3**, 094002 (2000), and references therein.
- [18] A. Fetterman, D. Mihalcea, S. Benson, D. Crawford, D. Edstrom, F. Hannon, P. Piot, J. Ruan, and S. Wang, *Nucl. Instrum. Methods Phys. Res., Sect. A* **1025**, 166051 (2022).
- [19] J. Qiang, *Phys. Rev. Accel. Beams* **21**, 114201 (2018).
- [20] Y. L. Cheon, S. H. Moon, M. Chung, and D. Jeon, *Phys. Plasmas* **27**, 063105 (2020).
- [21] C. Chen, R. Pakter, and R. C. Davidson, *Phys. Rev. Lett.* **79**, 225 (1997).
- [22] L. Groening, C. Xiao, and M. Chung, *Phys. Rev. Accel. Beams* **21**, 014201 (2018).
- [23] L. Groening, M. Maier, C. Xiao, L. Dahl, P. Gerhard, O. Kester, S. Mickat, H. Vormann, M. Vossberg, and M. Chung, *Phys. Rev. Lett.* **113**, 264802 (2014).
- [24] M. Reiser, *Theory and Design of Charged Particle Beams*, 2nd ed. (Wiley-VCH, Weinheim, 2008).
- [25] Y. K. Batygin, *Nucl. Instrum. Methods Phys. Res., Sect. A* **995**, 165074 (2021).
- [26] J. Qiang and R. D. Ryne, *Phys. Rev. Accel. Beams* **3**, 064201 (2000).
- [27] J.-M. Lagniel, Zero-current longitudinal beam dynamics, in *Proceedings of 27th Linear Accelerator Conference-LINAC14* (2014), pp. 572–574.
- [28] G. Stupakov, The U. S. Particle Accelerator School, Lansing, Michigan (2007).
- [29] H. Wiedemann, *Particle Accelerator Physics*, 4th ed. (Springer, Switzerland, 2015).
- [30] L. Groening, W. Barth, W. Bayer, G. Clemente, L. Dahl, P. Forck, P. Gerhard, I. Hofmann, M. Kaiser, M. Maier *et al.*, Experimental observation of space charge driven resonances in a linac, *Trans. Emittance Meas.* **40**, A1 (2010).
- [31] D. Uriot, N. Pichoff *et al.*, Status of TraceWin code, in *Proceedings of IPAC'15* (2015), pp. 92–94.
- [32] C. Allen and T. Wangler, *Phys. Rev. Accel. Beams* **5**, 124202 (2002).
- [33] P. Nghiem, N. Chauvin, M. Comunian, C. Oliver, W. Simeoni, D. Uriot, and M. Valette, *Laser Part. Beams* **32**, 639 (2014).
- [34] I. Hofmann and O. Boine-Frankenheim, *Phys. Rev. Lett.* **118**, 114803 (2017).
- [35] A. Rubin, L. Groening, and I. Hofmann, *Phys. Rev. Accel. Beams* **23**, 124202 (2020).
- [36] T. P. Wangler, *RF Linear Accelerators* (Wiley, New York, 2008).
- [37] P. A. P. Nghiem, N. Chauvin, W. Simeoni, Jr., and D. Uriot, *Appl. Phys. Lett.* **104**, 074109 (2014).
- [38] P. A. P. Nghiem, M. Valette, N. Chauvin, N. Pichoff, and D. Uriot, *Phys. Plasmas* **22**, 083115 (2015).
- [39] L. Groening, C. Xiao, and M. Chung, *Phys. Rev. Accel. Beams* **24**, 054201 (2021).